

Theoretical and experimental studies on high-power laser-induced thermal blooming effect in chamber with different gases

Xiangyizheng Wu(吴祥议政), Jian Xu(徐健), Keling Gong(龚柯菱), Chongfeng Shao(邵崇峰), Yang Kou(寇洋), Yuxuan Zhang(张宇轩), Yong Bo(薄勇),, and Qinjun Peng(彭钦军)

Citation: Chin. Phys. B, 2022, 31 (**8**): 086105. DOI: 10.1088/1674-1056/ac6165
Journal homepage: http://cpb.iphy.ac.cn; http://iopscience.iop.org/cpb

What follows is a list of articles you may be interested in

Sphere-shaped SiGe micro/nanostructures with tunable Ge composition and size formed by laser irradiation

Xinxin Li(李欣欣), Zhen Deng(邓震), Sen Wang(王森), Jinbiao Liu(刘金彪), Jun Li(李俊), Yang Jiang(江洋), Ziguang Ma(马紫光), Chunhua Du(杜春花), Haiqiang Jia(贾海强), Wenxin Wang(王文新), and Hong Chen(陈弘)
Chin. Phys. B, 2021, 30 (**9**): 096104. DOI: 10.1088/1674-1056/ac0347

Effects of Al component content on optoelectronic properties of $Al_xGa_{1-x}N$

Yan-Jun Ji(纪延俊), Jun-Ping Wang(王俊平), You-Wen Liu(刘友文)
Chin. Phys. B, 2018, 27 (**10**): 106102. DOI: 10.1088/1674-1056/27/10/106102

Slip on the surface of silicon wafers under laser irradiation:Scale effect

Zhi-Chao Jia(贾志超), Ze-Wen Li(李泽文), Jie Zhou(周洁), Xiao-Wu Ni(倪晓武)
Chin. Phys. B, 2017, 26 (**11**): 116102. DOI: 10.1088/1674-1056/26/11/116102

Mechanism of floating body effect mitigation via cutting off source injection in a fully-depleted silicon-on-insulator technology

Pengcheng Huang(黄鹏程), Shuming Chen(陈书明), Jianjun Chen(陈建军)
Chin. Phys. B, 2016, 25 (**3**): 036103. DOI: 10.1088/1674-1056/25/3/036103

A single-event transient induced by a pulsed laser in a silicon-germanium heterojunction bipolar transistor

Sun Ya-Bin, Fu Jun, Xu Jun, Wang Yu-Dong, Zhou Wei, Zhang Wei, Cui Jie, Li Gao-Qing, Liu Zhi-Hong, Yu Yong-Tao, Ma Ying-Qi, Feng Guo-Qiang, Han Jian-Wei
Chin. Phys. B, 2013, 22 (**5**): 056103. DOI: 10.1088/1674-1056/22/5/056103

Theoretical and experimental studies on high-power laser-induced thermal blooming effect in chamber with different gases

Xiangyizheng Wu(吴祥议政)[1,2,4], Jian Xu(徐健)[1,2,3,†], Keling Gong(龚柯菱)[1,2,3], Chongfeng Shao(邵崇峰)[1,2,3], Yang Kou(寇洋)[1,2,3], Yuxuan Zhang(张宇轩)[1,2,4], Yong Bo(薄勇),[1,2,3,‡] and Qinjun Peng(彭钦军)[1,2,3]

[1] *Key Laboratory of Solid-State Laser, Technical Institute of Physics and Chemistry, Chinese Academy of Sciences, Beijing* 100190, *China*

[2] *Key Laboratory of Functional Crystal and Laser Technology, Technical Institute of Physics and Chemistry, Chinese Academy of Sciences, Beijing* 100190, *China*

[3] *Institute of Optical Physics and Engineering Technology, Qilu Zhongke, Jinan* 250000, *China*

[4] *University of Chinese Academy of Sciences, Beijing* 100190, *China*

(Received 11 January 2022; revised manuscript received 22 March 2022; accepted manuscript online 28 March 2022)

High-power laser induced thermal blooming effects in a closed chamber with three different gases are investigated theoretically and experimentally in this work. In the theoretical treatment, an incompressible gas turbulent model is adopted. In the numerical simulation the gas refractive index as a function of both the temperature and pressure is taken into consideration. In the experimental study the pump-probe technology is adopted. A high-power 1064-nm fiber laser with maximum output power of 12 kW is used to drive the gas thermal blooming, and a 50-mW high-beam-quality 637-nm laser diode (LD) is used as a probe beam. The influences of the gas thermal blooming in the chamber on the probe beam wavefront and beam quality are analyzed for three different gases of air, nitrogen, and helium, respectively. The results indicate that nitrogen is well suitable for restraining thermal blooming effect for high-power laser. The measured data are in good agreement with the simulated results.

Keywords: laser radiation, numerical simulation, propagation, thermal blooming

PACS: 61.80.Ba, 44.05.+e, 44.10.+i, 47.27.–i **DOI:** 10.1088/1674-1056/ac6165

1. Introduction

High output power and high beam quality lasers that can be used in laser combination are potentially required in beam application.[1] With the progressive scaling up of laser output power, the thermal blooming effect in a closed chamber becomes an important research subject. It is easy for high power laser to induce the temperatures of the mirrors, airflow and chambers to rise, which is the main source of creating the temperature gradients. These gradients commonly cause the refractive index to be distributed unevenly, which eventually degrading both the wavefront quality and the beam quality of lasers.[2] For example, the air contains suspended dust, droplets and other solid or liquid particles, which are called aerosols. These aerosols have strong absorption in near-infrared region.[3] Primitively, the thermal blooming effect in gas was discovered along with the phenomenon research of laser propagation in the liquid.[4] In order to eliminate the thermal blooming effect, the experimental investigation and numerical analysis were carried out in the laser chamber with gas-flow.[5,6] Several methods were employed to suppress the thermal blooming effect in the chamber. A more effective way was to inject the gas with low absorption coefficient into the chamber. For example, the dry nitrogen was injected into the Navy-ARPA chemical laser (NACL) emission system to restrain the heat accumulation in the chamber.[7] To reduce the weight of the optical system, the non-flowing gas was adopted. Because helium has the properties of high thermal diffusivity and low absorption coefficient, helium was used as the medium in the non-flowing working mode. According to the study of the thermal blooming phenomenon of laser beam propagation in the chamber with static gas, the optical path difference (OPD) of laser beam in the non-flowing helium is better than that in the medium flow system under the same wall conditions.[8] Meanwhile, the numerical simulations were used to calculate the thermal blooming. For instance, the beam propagation was simulated by paraxial equation, and the incompressible Navier–Stokes equation was used in fluid medium.[9] Using the weakly compressible fluid model and the scalar wave equation, the influence of gas thermal effect on laser propagation in a closed tube filled with air was studied numerically. The results show that the weakly compressible fluid model is more suitable for solving the problems with complex boundary conditions.[10] In order to correct the wavefront distortion of laser beam caused by thermal blooming, an adaptive optical system model was established.[11] Recently, the thermal coupling effect of pipelines with different complex structures on laser propagation has also been studied.[12] Moreover, the axial flow and outlet suction methods were used to reduce the thermal blooming effect.[13]

†Corresponding author. E-mail: xujian208@mails.gucas.ac.cn

‡Corresponding author. E-mail: boyong@tsinghua.org.cn

© 2022 Chinese Physical Society and IOP Publishing Ltd

However, for most of thermal blooming investigations in the chamber or the tube, the lasers have relatively low power or energy[2,11–13] and there have been less reports on the influence of thermal looming on the beam quality. In this work, the thermal blooming effect caused by a 10-kW laser in a chamber is studied theoretically and experimentally. We examine the influences of the thermal blooming effect on the beam wavefront distribution and the beam quality when the chamber is filled with air, nitrogen, and helium, respectively. The simulation results are compared with the experimental data.

2. Theoretical framework

The optical path difference (OPD) of the laser beam caused by the gas thermal blooming effect in the chamber can be expressed as

$$\mathrm{OPD} = \int \Delta n \cdot \mathrm{d}s, \tag{1}$$

where Δn is the change in the refractive index of the gas medium, and S is the length of the light path. For ideal gas, the gas equation of state can be described as[14]

$$PV/RT \approx 1 - \varepsilon p, \tag{2}$$

where P is the pressure with the Pascal (Pa), V is the volume, R is the gas constant, T is the temperature in Kelvin (K), and ε is a polynomial of temperature.[15,16]

Starting from the Lorentz–Lorenz formula, another equation of gas refractive index can be obtained below:[17]

$$(n-1) = DK, \tag{3}$$

$$D \approx \frac{P\left[1+\varepsilon P+\dfrac{KP}{6(1+\alpha T)}\right]}{(1+\alpha T)}, \tag{4}$$

where D is the molecule density of gas, $\alpha = 1/273.15$ K, and the dispersion factor $K \approx (n-1)(1+\alpha T/P)$, and the value of K can be obtained by using the gas refractive index measured under the standard condition ($T = 293.15$ K and $P = 101325$ Pa, *i.e.*, 1 atm, 1 atm = 1.01325×10^5 Pa).

Using Eq. (3), the gas refractive index equation under different environmental conditions can be deduced by the gas refractive index under standard condition as follows:

$$(n-1) = \frac{D}{D_\mathrm{s}}(n_\mathrm{s}-1), \tag{5}$$

where the subscript s represents the parameter under the standard condition.

As is well known, the gas refractive index under standard condition is[18]

$$(n_\mathrm{s}-1)\times10^8 = A_0 + \frac{A_1}{\left(B_1-\dfrac{1}{\lambda^2}\right)} + \frac{A_2}{\left(B_2-\dfrac{1}{\lambda^2}\right)}, \tag{6}$$

where A, A_1, A_2, B_1, and B_2 are constants, and λ is the wavelength. For air, $A = 8015.514$, $A_1 = 2368616$, $A_2 = 19085.73$, $B_1 = 128.7459$, and $B_2 = 50.01974$.[15] For nitrogen, $A = 8736.28$, $A_1 = 2398095.2$, $A_2 = 0$, $B_1 = 128.7$, and $B_2 = 0$.[15] For helium, $A = 0$, $A_1 = 1470091$, $A_2 = 0$, $B_1 = 423.98$, and $B_2 = 0$.[16]

Combining the above Eqs. (4)–(6), the refractive index of the gas medium, n, induced by thermal blooming can be expressed as

$$n \approx \left[\frac{P\left[1+\varepsilon P+\dfrac{KP}{6(1+\alpha T)}\right]}{(1+\alpha T)D_\mathrm{S}}\right] \times\left[\left(A_0+\frac{A_1}{\left(B_1-\dfrac{1}{\lambda^2}\right)}+\frac{A_2}{\left(B_2-\dfrac{1}{\lambda^2}\right)}\right)\times10^{-8}\right]+1. \tag{7}$$

Then, the change of refractive index Δn can be obtained as follows:

$$\Delta n = n - n_\mathrm{s}. \tag{8}$$

It can be seen from Eqs. (7) and (8), at a specific wavelength, the change of refractive index of gas is related to the distribution of the gas temperature and pressure. Therefore, to calculate the refractive index distribution of gas and the distribution of OPD, we need to examine the distributions of temperature and pressure.

In this work, the incompressible turbulent K–ε model for the gas propagation in the chamber is used. The corresponding fluid equations are as follows:[13]

$$\frac{\partial\rho}{\partial t} + \nabla(\rho v) = 0, \tag{9}$$

$$\frac{\partial v}{\partial t} + v\cdot\nabla v = -\frac{1}{\rho}\nabla p + g, \tag{10}$$

$$\frac{\partial\rho T}{\partial t} + \nabla\cdot(\rho v T) = \nabla\cdot\left(\frac{K}{\rho C_\mathrm{p}}\nabla T\right) + \frac{Q}{\rho C_\mathrm{p}}, \tag{11}$$

where ρ, v, and g respectively represent the density, velocity vector, and gravity of the gas, K is the thermal conductivity of the gas, C_p is the specific heat capacity of the gas at constant pressure, and Q is the heat source which the laser irradiation acts as. Also, the influence of gravity is taken into consideration.

3. Experimental description

Figure 1 shows the experimental arrangement based on the pump–probe technology for the observation of the thermal blooming effect. A high-power 1064-nm quasi-continuous wave (QCW) fiber laser (GM:5M-120HC) was used as a pump source to produce the thermal blooming. The 1064-nm laser delivers maximum output power of 12 kW. The 1064-nm beam is collimated with a diameter of 15 mm via a relay optics. A 50-mW 637-nm CW laser diode (THORLABS LP637-SF70) with high beam quality of $\beta \sim 1.09$ is used as a probe beam.

The 637-nm beam is also collimated into a 15-mm diameter beam through another relay optics. In Fig. 1, M1 is a dichroic mirror with high transmissivity at 1064 nm and high reflectivity at 637 nm. The probe beam is added to 1064-nm beam by dichroic mirror M1, then the resulting beam propagates into the chamber. Plane mirrors M2 and M3 with a distance of 3000 mm in between are highly reflective at 1064 nm and 637 nm, they being placed in the chamber. Both the 1064-nm beam and the probe beam are reflected between the two mirrors four times, with total optical path arriving at 15000 mm. The laser beams exited from the chamber are separated by a beam splitter. Thus the probe beam is divided into 2 subbeams by another beam splitter. The wavefront distortion and beam quality of the probe beam are measured simultaneously with a Hardman wavefront sensor and a charge coupled device (CCD) camera, respectively. The chamber is filled with air, nitrogen, and helium at room-temperature (RT) and 1 atm, respectively.

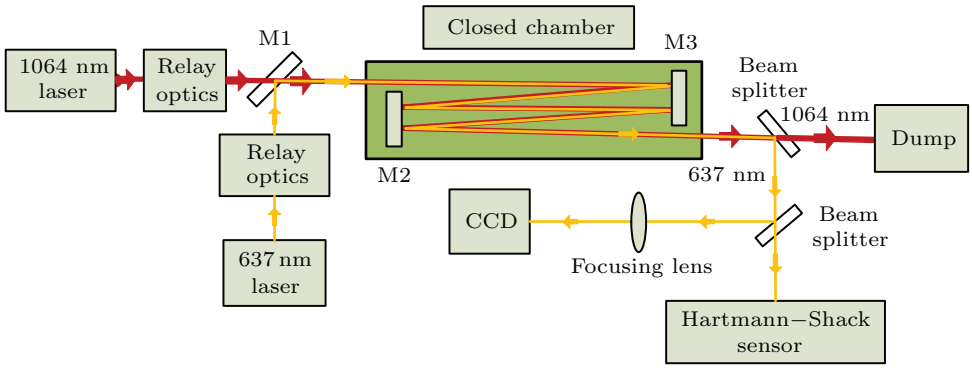


Fig. 1. Experimental arrangement of thermal blooming effect.

4. Results and discussion

In the observation of the thermal blooming, different pump power value take 0.5, 1.0, 4.0, and 8.0 kW over 100 s, respectively. The beam radius of the pump beam and the probe beam in the chamber window are both 7.5 mm. Consequently, the corresponding pump power densities are 283, 566, 2264, and 4527 W/cm^2, respectively. The initial temperature and pressure of the chamber are 20 °C and 1 atm, the initial refractive index of air, nitrogen, and helium are 1000272, 1.000277, and 1.000035, respectively. The isobaric heat capacity of air, nitrogen, and helium are 1015, 1039, and 5196 J/(kg·K), respectively. The thermal conductivity of air, nitrogen, and helium are 0.0256, 0.025, and 0.149 W/(m·K), respectively. The absorption coefficient of air at 1064 nm is $\alpha = 1.5 \times 10^{-7}$ cm^{-1}.[19] Because nitrogen and helium have extremely low absorption coefficient at 1064 nm, their absorption can be omitted. On the other hand, the laser energy absorbed by the reflective mirror is 10 ppm. The convective heat flux between the chamber and the external gas is 10 W/(m^2·K). The flow field is simulated by incompressible turbulent K–ε model as mentioned above, and the OPD and wavefront distribution of the light field are simulated by ray tracing method based on a COMSOL Multiphysics software in the approximation of the flat top beam. Moreover, the beam quality β is estimated with the ZEMAX software based on the beam intensity distribution. The experimental and simulation results are shown in Fig. 2.

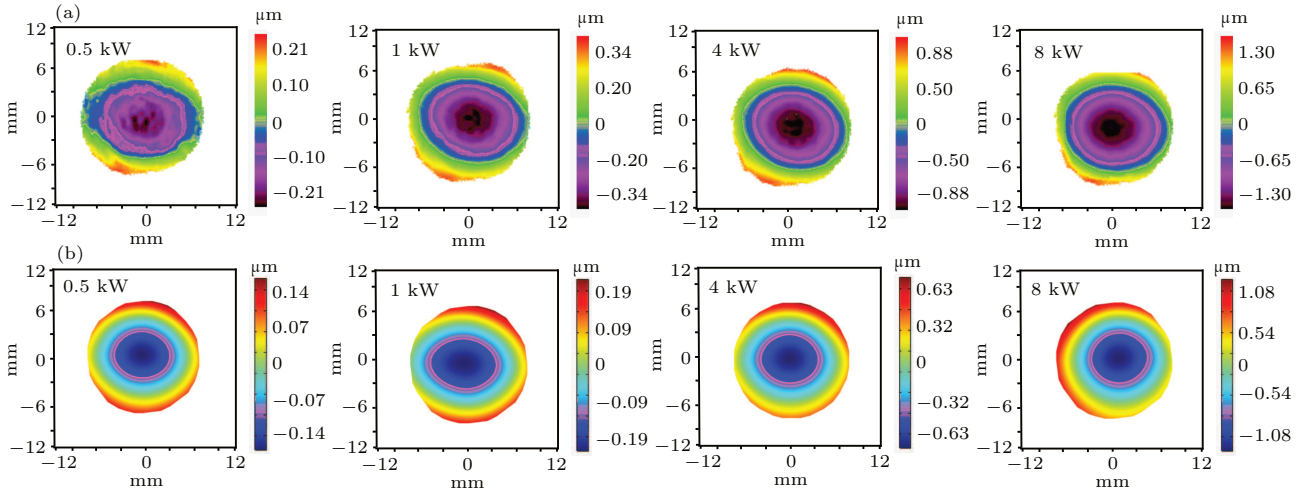


Fig. 2. (a) Measured and (b) simulated wavefront distributions of probe beam exited from chamber filled with air under different pump power values of 0.5, 1.0, 4.0, and 8.0 kW at the 100th second.

Figure 2 shows the measured and simulated wavefront distributions of the probe beam exited from the chamber filled with air under different pump power values of 0.5, 1.0, 4.0, and 8.0 kW at the 100th second. It can be obtained from Fig. 2(a) that the measured peaktovalley (PV) values of the wavefront distortion are 0.43, 0.69, 1.8, and 2.6 μm for the pump power values of 0.5, 1.0, 4.0, and 8.0 kW, respectively. From Fig. 2(b), the corresponding simulated PV values are 0.28, 0.38, 1.3, and 2.2 μm.

Figure 3 shows the measured and simulated far-field beam intensity distributions of the probe beam exited from the chamber filled with air under different pump power values of 0.5, 1.0, 4.0, and 8.0 kW at the 100th second. It can be deduced from Fig. 3(a) that the measured values of beam quality $\beta_{\text{m_Air}}$ are 1.6, 2.7, 4.6, and 5.6 for the pump power values of 0.5, 1.0, 4.0, and 8.0 kW, respectively. Similarly, from Fig. 3(b), the corresponding simulated values of beam quality $\beta_{\text{s_Air}}$ are 1.5, 2.3, 4.3, and 5.1.

Figure 4 shows the measured and simulated wavefront distributions of the probe beam exited from the chamber filled with nitrogen under different pump power values of 0.5, 1.0, 4.0, and 8.0 kW at the 100th second. It can be extracted from Fig. 4(a) that the measured PV values of the wavefront distortion are 0.11, 0.14, 0.11, and 0.18 μm for the pump power values of 0.5, 1.0, 4.0, and 8.0 kW, respectively. From Fig. 4(b), the simulated PV values of the wavefront distortion are 0.001, 0.004, 0.011, and 0.025 μm for the pump power values of 0.5, 1.0, 4.0, and 8.0 kW, respectively.

Figure 5 shows the measured and simulated far-field beam intensity distributions of the probe beam exited from the chamber filled with nitrogen under different pump power values of 0.5, 1.0, 4.0, and 8.0 kW at the 100th second. Figure 5(a) shows that the measured values of beam quality $\beta_{\text{m_N}_2}$ are 1.10, 1.11, 1.13, and 1.13 for the pump power values of 0.5, 1.0, 4.0, and 8.0 kW, respectively. Figure 5(b) shows that the values of simulated beam quality $\beta_{\text{s_N}_2}$ are 1.002, 1.003, 1.004, and 1.006 for the pump power values of 0.5, 1.0, 4.0, and 8.0 kW, respectively.

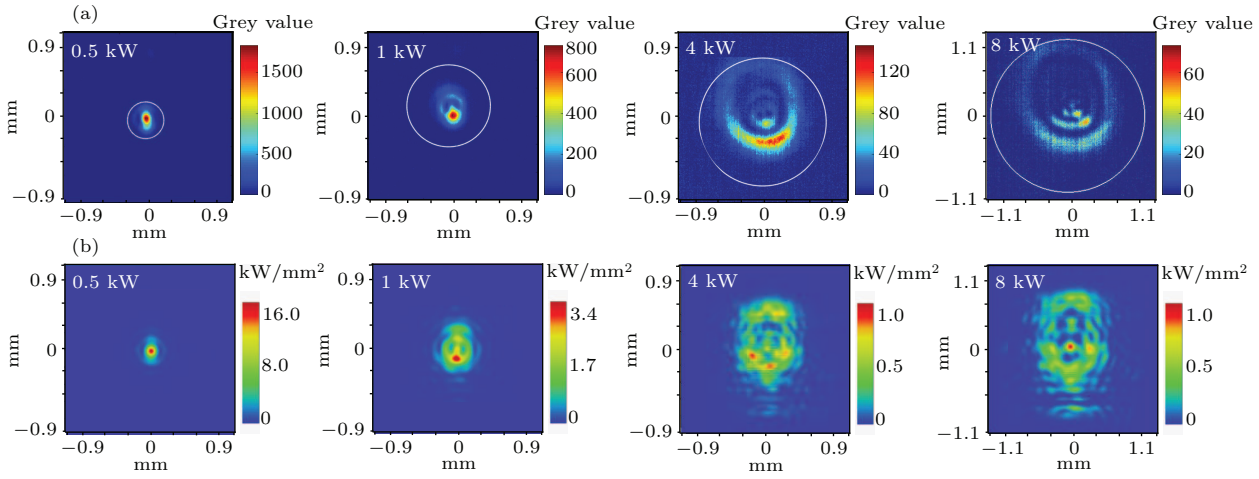


Fig. 3. (a) Measured and (b) simulated far-field beam intensity distributions of probe beam exited from chamber filled with air under different pump power values of 0.5, 1.0, 4.0, and 8.0 kW at the 100th second.

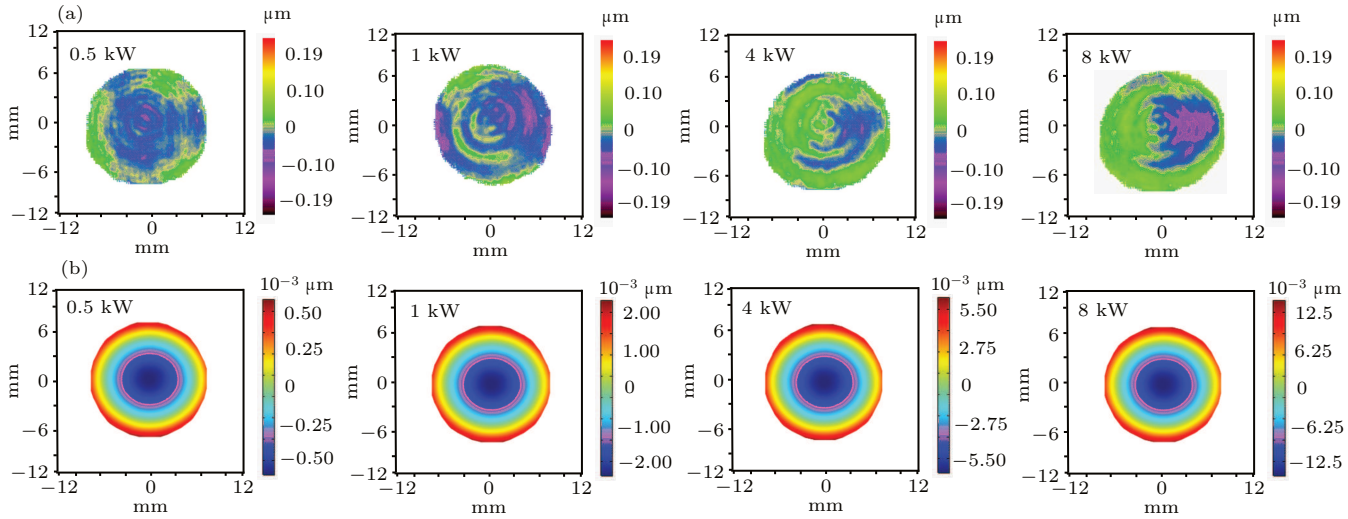


Fig. 4. (a) Measured and (b) simulated wavefront distributions of probe beam exited from chamber filled with nitrogen under different pump power values of 0.5, 1.0, 4.0, and 8.0 kW at the 100th second.

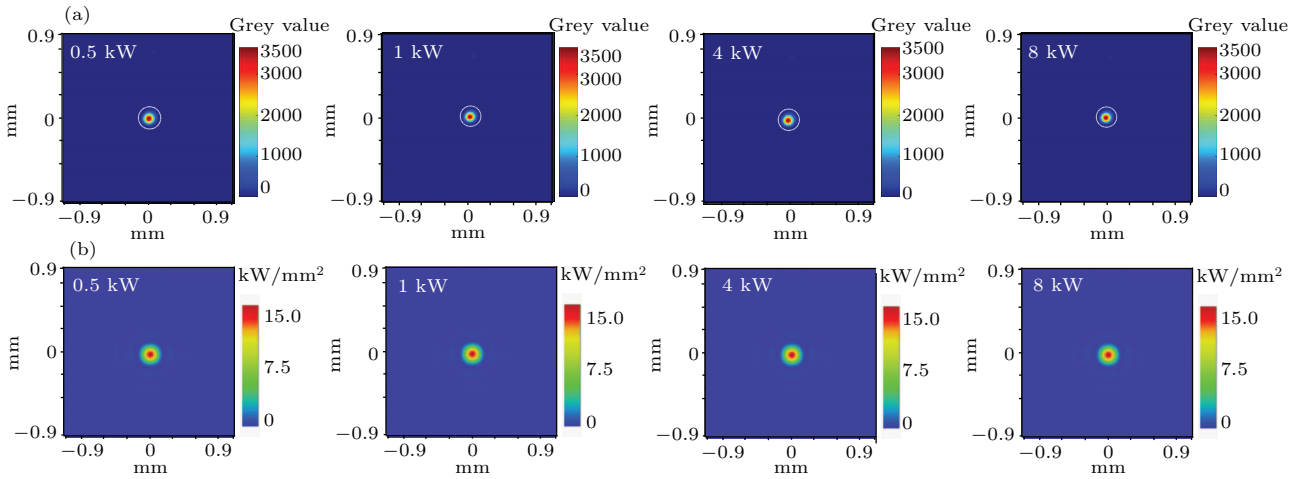


Fig. 5. (a) Measured and (b) simulated far-field beam intensity distributions of probe beam exited from chamber filled with nitrogen under different pump power values of 0.5, 1.0, 4.0, and 8.0 kW at the 100th second.

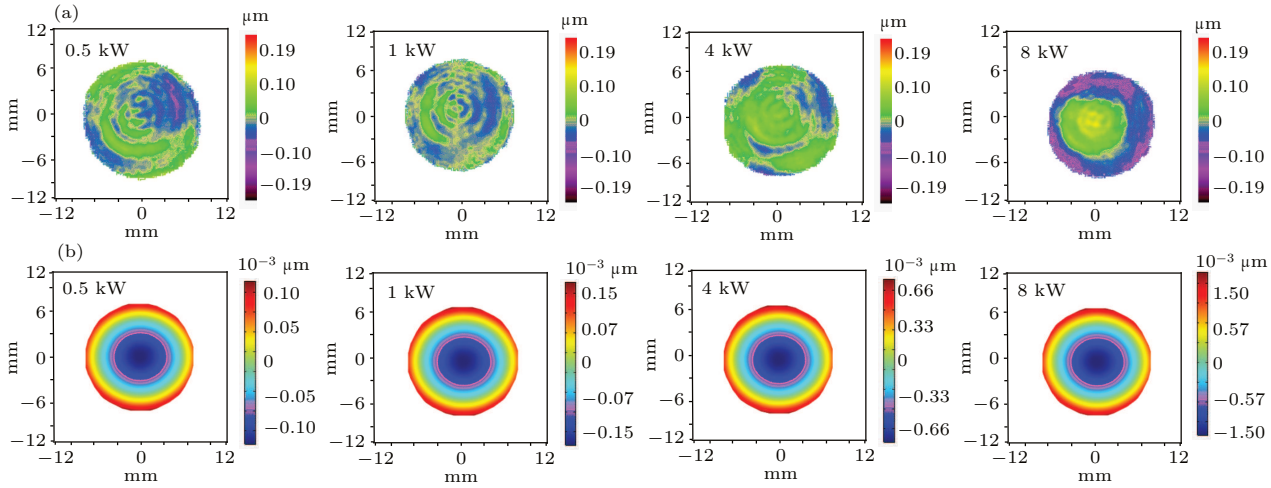


Fig. 6. (a) Measured and (b) simulated wavefront distributions of probe beam exited from chamber filled with helium under different pump powers of 0.5, 1.0, 4.0, and 8.0 kW at the 100th second.

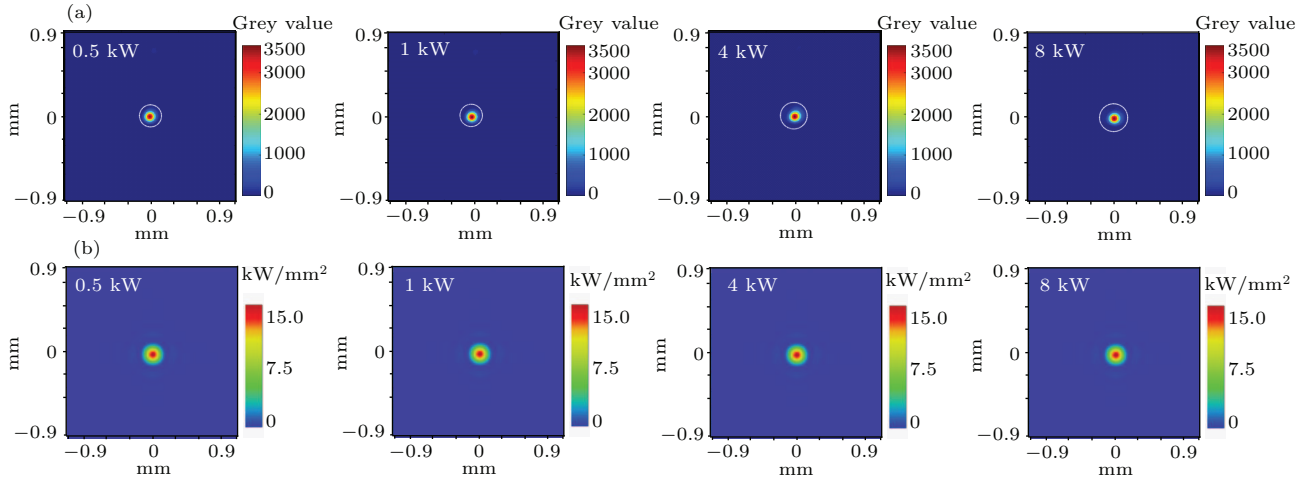


Fig. 7. (a) Measured and (b) simulated far-field beam intensity distributions of probe beam exited from chamber filled with helium under different pump power values of 0.5, 1.0, 4.0, and 8.0 kW at the 100th second.

Figure 6 shows the measured and simulated wavefront distributions of the probe beam exited from the chamber filled with helium under different pump power values of 0.5, 1.0, 4.0, and 8.0 kW at the 100th second. It is created from Fig. 6(a) that the measured PV values of the wavefront distortion are 0.135, 0.142, 0.136, and 0.21 μm for the pump power values of 0.5, 1.0, 4.0, and 8.0 kW, respectively. Form Fig. 6(b), the simulated PV values of the wavefront distortion are 0.0002, 0.0003, 0.0013, and 0.003 μm for the pump power values of 0.5, 1.0, 4.0, and 8.0 kW, respectively.

Figure 7 shows the measured and simulated far-field beam intensity distributions of the probe beam exited from the chamber filled with helium under different pump power values of 0.5, 1.0, 4.0, and 8.0 kW at the 100th second. From Fig. 7(a), the measured values of beam quality $\beta_{\text{m_He}}$ are 1.13, 1.13, 1.16, and 1.34 for the pump power values of 0.5, 1.0, 4.0, and 8.0 kW, respectively. From Fig. 7(b), when the pump power values are 0.5, 1.0, 4.0, and 8.0 kW, the simulated values of beam quality $\beta_{\text{s_He}}$ are 1.002, 1.002, 1.002, and 1.0025, respectively.

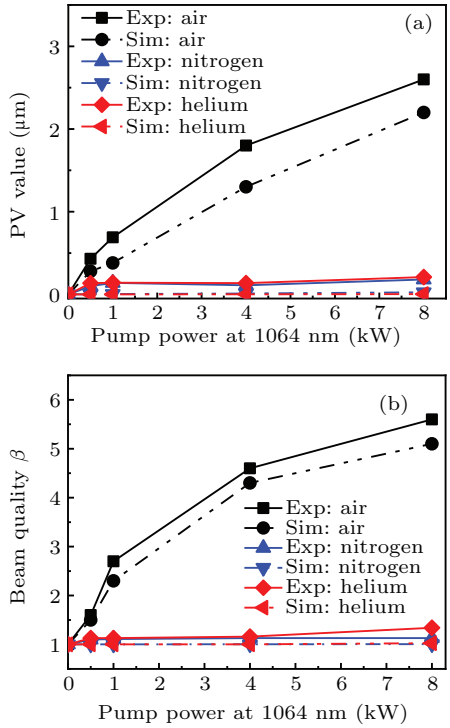


Fig. 8. Measured and simulated (a) PV values of wavefront distortion and (b) values of beam quality β of probe beam *versus* pump power for different gases, with solid line representing measured results, dashed line denoting simulated results, black line, blue line, and red line for the results of air, nitrogen, and helium, respectively.

Figures 8(a) and 8(b) show the comparison between the measured and simulated PV values of the wavefront distortion and the values of beam quality β of the probe as a function of pump power for different gases, respectively. It is found from Fig. 8 that the measured PV values of the wavefront distortion and the values of beam quality β are in good agreement with the simulated results for corresponding gases. When the chamber is filled with air and the pump power value increases from 0.5 kW to 8.0 kW, the measured PV values of the wavefront distortion and the values of beam quality $\beta_{\text{m_Air}}$ increase quickly with the pump power increasing, they increased 6.0 and 3.5 times, respectively. For the nitrogen, the measured PV values of the wavefront distortion and the values of beam quality $\beta_{\text{m_N}_2}$ increase slightly with the pump power increasing, they increased 1.8 and 1.03 times for pump power increasing from 0.5 kW to 8.0 kW, respectively. As for the helium, the measured PV values of the wavefront distortion and the values of beam quality $\beta_{\text{m_He}}$ increase progressively with the pump power, they increased from 1.56 and 1.19 times for pump power increasing from 0.5 kW to 8.0 kW, respectively. Clearly, the nitrogen and helium are more suitable gas media than air for mitigating the thermal blooming. At the pump power value of 8.0 kW, the measured PV value of the wavefront distortion and the value of beam quality $\beta_{\text{m_He}}$ for helium are slightly larger than the simulated results. It may be that a little air is mixed into the chamber due to the fact that helium with smaller molecular mass is easy to escape from the chamber, because the poor-sealing chamber is used in our experiment. Consequently, although nitrogen and helium both have lower absorption to the pump laser than air, nitrogen is more suitable to serve as the filling gas of the poor-sealing-requirement chamber, as a result of its lower requirements for the sealing degree of the chamber than helium.

5. Conclusions

In this work, the simulation and experiment research about high-power laser-induced the thermal blooming effect in the chamber are carried out by the pump–probe method. The influence of the gas thermal blooming on the laser wavefront and the beam quality are investigated and those results for the chamber filled with air, nitrogen, and helium are compared with each other correspondingly. The experimental results are basically in agreement with the numerical simulation. The results confirm that the nitrogen can effectively alleviate the thermal blooming effect in a laser system.

Acknowledgement

Project supported by the National Natural Science Foundation of China (Grant No. 61875208).

References

[1] Gong K L, Xu J, Zhang L, Guo Y D, Wang B S, Yang L, Li S, Chen Z Z, Yuan L, Kou Y, Xu Y T, Peng Q J and Xu Z Y 2019 *Chin. Phys. Lett.* **36** 074204
[2] Lu L, Wang Z Q, Zhang P F, Qiao C H and Cai Y J 2021 *Opt. Lett.* **46** 4304
[3] Zhu W Y, Qian X M, Rao R Z and Wang H H 2019 *Infrared and Laser Engineering* **48** 12 (in Chinese)
[4] Rieckhoff K E 1966 *Appl. Phys. Lett.* **9** 87
[5] Valley G C, Shen L W and Kelly R E 1979 *Appl. Opt.* **18** 2728
[6] McClellan C, Munn M W and Nourie D 1979 *Appl. Opt.* **18** 3984
[7] Albertine J R, Siahatgar S and Bennett H E 1997 *Proc. SPIE* **2988** 257
[8] Shen P I and Andrepont M 2000 *Proc. SPIE* **4034** 100
[9] Benjamin F A and Jonah A R 2019 *J. Electromagn. Waves Appl.* **33** 96
[10] Liu J and Wang S Q 2011 *Adv. Mater. Res.* **354–355** 165
[11] Kanev F, Makenova N, Nesterov R and Izmailov I 2016 *Mater. Sci. Eng.* **124** 012063
[12] Yu H H, Hu P, An J Z and Zhang F Z 2015 *Proc. SPIE* **9255** 92552Z-1
[13] Zu F Y, Wang J H, Ren G, Tan Y F, Zhu N B and Ai Z W 2016 *Proc. SPIE* **9682** 96820T-1
[14] Peck E R and Khanna B N 1996 *J. Opt. Soc. Am.* **56** 1059
[15] Zhang J, Liu Z H and Wang L J 2008 *Appl. Opt.* **47** 3143
[16] Mansfield C R and Peck E R 1969 *J. Opt. Soc. Am.* **59** 199
[17] Bonsch G and Potulski E 1998 *Metrologia* **35** 133
[18] Zhang J, Lu Z H, Menegozzi B and Wang L J 2006 *Rev. Sci. Instrum.* **77** 083104
[19] Wang Y J, Fan C Y and Wei H L 2015 *Laser Beam Propagation and Applications through the Atmosphere and Sea Water* (Beijing: Nation Defense Industry Press) pp. 312–313 (in Chinese)